Electronic Supplementary Material (ESI) for Materials Advances.

Supplementary Information:

Ab Initio Study of Uniaxial Strain-Induced Thermoelectric Property Tuning of Individual Single-Wall Carbon Nanotubes

Md. Mafizul Islam[1,2] and Ahmed Zubair[1,*]

[1]Department of Electrical and Electronic Engineering, Bangladesh University of Engineering and Technology, Dhaka 1205, Bangladesh.

[2]Department of Textile Machinery Design and Maintenance, Bangladesh University of Textiles, Dhaka 1208, Bangladesh.

[*]ahmedzubair@eee.buet.ac.bd

S1 Band structures of (11,0) SWCNT under uniaxial strain

We calculated the band structures of (11,0) SWCNT at the relaxed state, evinced 0.8 eV. We modeled the strained SWCNT by introducing uniaxial strains parallel to the tube axis. Within a smaller range (from -3% to +6%) of uniaxial strains, the band gap change occurred with a negative slope of variation as seen in Figure S1. However, beyond this strain range, the band gap started to vary in a zigzag pattern. The band gap alteration occurred with a shifting of conduction band minima (CBM) and valence band maxima (VBM), as can be seen in Figure S1(h). The energy dispersion cones **K** and **K′** ($\mathbf{K}_i$), and the allowed **k** states moved due to strain introduced along the tube's axial direction. When the nearest **k** state came closer to $\mathbf{K}_i$, the band gap decreased and widened while their spacing increased. The peak of the band gaps (1.05 eV) was obtained while the $\mathbf{K}_i$ points resided exactly at the mid of two adjacent **k** states, which was the critical position. The spacing between the $\mathbf{K}_i$ points and the nearest **k** state alternated with a zigzag pattern when it crossed the critical position. Consequently, the band gap varied with the zigzag pattern. Within our studied strain range, the (11,0) SWCNT went through a semiconductor-metal transition state at 6% tensile strain and was expected to occur again beyond 9% compressive strain.

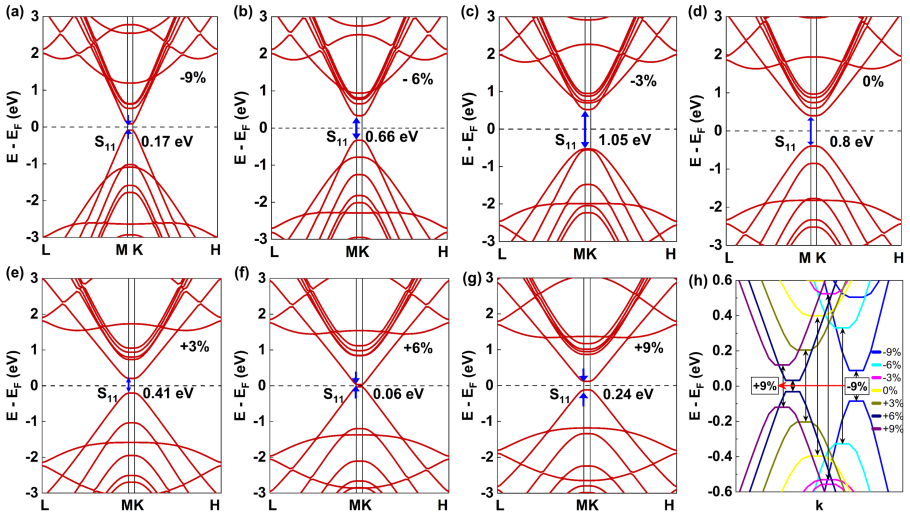

Figure S1: Band structures of (11,0) SWCNT at different strains– (a) -9%, (b) -6%, (c) -3%, (d) 0% (relaxed state), (e) +3%, (f) +6%, and (g) +9%. The Fermi level E_F shifted to 0 eV. (h) A zoomed-in view of CBM and VBM, where the shifting of Dirac cones of energy dispersion due to uniaxial strain are apparent.

S2 Band structures of (9,0) SWCNT under uniaxial strain

The quasi-metallic type (9,0) SWCNT, which lies under the classification of $(n, 0)$ with n being an integer multiple of 3, revealed a curvature-induced small band gap 0.19 eV (see in Figure S2). Applying uniaxial stress along the tube axis, which was modeled by percentage strain, showed an increasing trend of band gap change until the spacing between $\mathbf{K}_i$ and $\mathbf{k}$ line reached its maximum. Beyond the critical position of $\mathbf{K}_i$ points in between the neighboring $\mathbf{k}$ lines, the band gap started to decrease. Consequently, a zigzag pattern of band gap variation formed, as obtained for (11,0) SWCNT. The maximum band gap (1.16 eV) was achieved at 9%

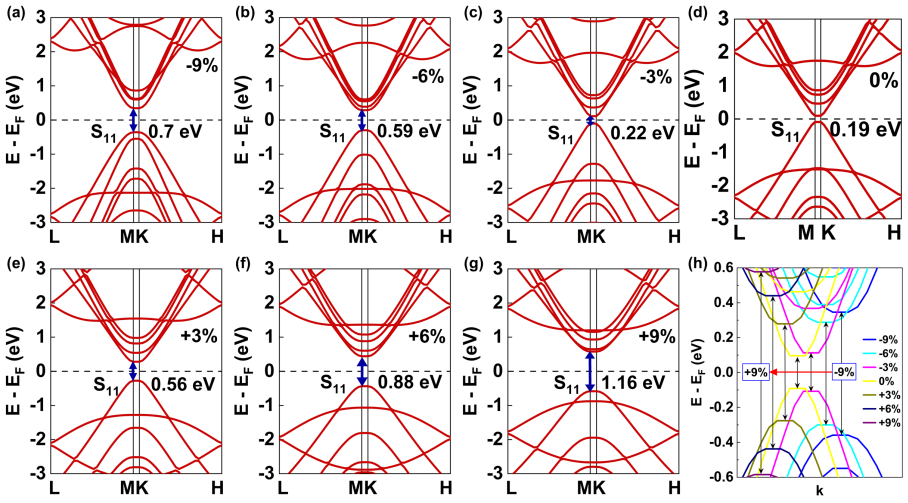

Figure S2: Band structures of (9,0) SWCNT at different strains– (a) -9%, (b) -6%, (c) -3%, (d) 0% (pristine), (e) +3%, (f) +6%, and (g) +9%. The Fermi level E_F shifted to 0 eV. (h) An expanded figure of CBM and VBM, where the energy dispersion cones were shifted due to uniaxial strain.

S3 Opposite slope of band gap alteration for (10,0) and (11,0) SWCNTs due to uniaxial strain

For elaborate explanation, we drawn an exaggerated graphical view of the sampling of first Brillouin zones (BZ) of $(n, 0)$ SWCNTs, where $n = 3i + j$ as shown in Figure S3. Particularly in this work, (10,0) SWCNT belongs to $j = +1$ and (11,0) SWCNT belongs to $j = -1$. The vertical solid lines are allowed $\mathbf{k}$

lines and the vertical dotted lines were drawn just for explanation, which was positioned at the middle of two adjacent **k** lines. Here we define the level of uniaxial strain required to shift the position of Dirac points onto the dotted lines as critical strain (ϵ_c). The Dirac points moved outward direction when the SWCNT underwent a uniaxial tensile strain, and the opposite (inward movement) action occurred for compressive strain. When an SWCNT of $j = +1$ underwent through a tensile strain, the spacing between a Dirac point and the nearest **k** line (Δk) increased till the tensile strain reached to ϵ_c. Since the band gap (E_g) of single wall carbon nanotubes (SWCNT) changes proportionally with Δk, hence the E_g of $j = +1$ SWCNT increased with tensile strain till the Dirac points reached the middle of two adjacent **k** lines, increasing the Δk at its maximum. If the strain is further increased ($> \epsilon_c$), the Dirac point cross the dotted vertical line and Δk starts to decrease, because, now the Δk is formed with other allowed **k** line. Hence, the band gap decreases i.e., band gap variation shows opposite trend.

However, for $j = -1$ SWCNT, the sampling of BZ is such that, upon applying uniaxial tensile strain along the tube's axial direction, the Dirac points moved outward direction and the Δk started to decrease and became zero (0) when the Dirac points reached to next allowed **k** line. Hence, the E_g of $j = -1$ SWCNT decreased with tensile strain, which is opposite to $j = +1$ SWCNT. If the strain is further increased, the Dirac point crosses the nearest allowed **k** line and Δk starts to increase. Hence, the band gap increases i.e., band gap variation shows opposite trend.

In summary, $j = +1$ and $j = -1$ SWCNTs show opposite trend of band gap alteration due to uniaxial strain.

S4 Impact of uniaxial strain on thermoelectric properties of (10,0) SWCNT

In Figure S4, we plotted the calculated results of the thermoelectric (TE) transport parameters such as electrical conductivity σ, Seebeck coefficient S, and thermoelectric power factor PF as a function of chemical potential. The TE transport parameters depend upon the electronic density of states (DOS), which was calculated with a large number of k-grid along the tube axis to ensure the higher accuracy of the calculations. The dos curve of (10,0) SWCNT validated the electronic band gaps obtained from its band structures at different strains. The band gap and S varied following a similar trend, with a broader range of tunability from 210 $\mu V\,K^{-1}$ (at -6%) to 1580 $\mu V\,K^{-1}$ (at +3%). The σ increased upon increasing compressive strain. However, the number of electronic energy states remained unaltered because of higher electron mobility caused by reduced electron effective mass, as can be associated with its band structure, where the band curvature at CBM became more narrow. At the same time, it underwent compressive strains. The peaks of TE PF ($S^2\sigma$) were obtained at the chemical potential where the peak of the absolute value of S occurred beyond the for-

bidden energy region because of no electronic states in that energy region. The enhancement of TE PF (~ 1.15 mW m^{-1} K^{-2}) was achieved for n-type carriers at 3% compressive strain as can be seen in Figure S4(c).

S5 TE transport properties of (9,0) SWCNT under uniaxial strain

We calculated the transport properties of (9,0) SWCNT at a similar method adopted for (10,0) SWCNT and plotted in Figure S5. The maximum value of S (1580 µV K^{-1}) achieved at 9% tensile strain. The σ was improved due to an increased number of electronic energy states for n-type carriers. The highest PF ($\sim$ 1.3 mW m^{-1} K^{-2}) was obtained for p-type carriers at 3% compressive strain.

S6 TE transport properties of (6,6) SWCNT under uniaxial strain

Owing to purely metallic characteristics of (6,6) SWCNT, a large value of σ was inherently obtained and increased upon introducing compressive strain. The PF was comparatively higher than that was obtained for semiconducting SWCNTs as studied here, due to its high electrical conductivity at room temperature, and it increased to 2.2 mW m^{-1} K^{-2} for p-type carriers while it underwent 9% compressive strain (see Figure S6).

S7 The change of TE properties with temperature for (10,0) SWCNT under uniaxial strain at particular dopant concentration

We calculated the TE transport parameters σ, PF, electronic thermal conductivity κ_e and the figure of merit zT with respect to temperature for (10,0) SWCNT at -3%, 0%, and +6% uniaxial strains for both types of carriers and plotted in Figure S7. The carrier concentration was chosen where they showed enhanced performance as TEG. The σ was little impacted at elevated temperature. The n-type dopants (N_D) on (10,0) SWCNT revealed dominating performance in σ at all temperatures. The σ increased slightly with temperature for the relaxed n-type (10,0) SWCNT. The σ and S dependent quantity TE PF of (10,0) SWCNT increased significantly above 600 K temperature at 3% compressive strain with 1.6×10^{20} cm^{-3} donor concentration. However, PF degraded at -3% and +6% strains with increasing temperature at 8.8×10^{19} cm^{-3} and 1.7×10^{20} cm^{-3} acceptor dopants concentrations, respectively.

The electronic thermal conductivity κ_e demonstrated an improved performance with temperature at 6% tensile strain at a donor concentration of 8.9 $\times$

10^{19} cm^{-3}. The zT factor showed an enhanced performance at room temperature. However, the zT enhancement occurred above 600 K temperature since the PF was increased and the κ_e was reasonably less at 3% compressive strain with 1.6×10^{20} cm^{-3} donor concentration.

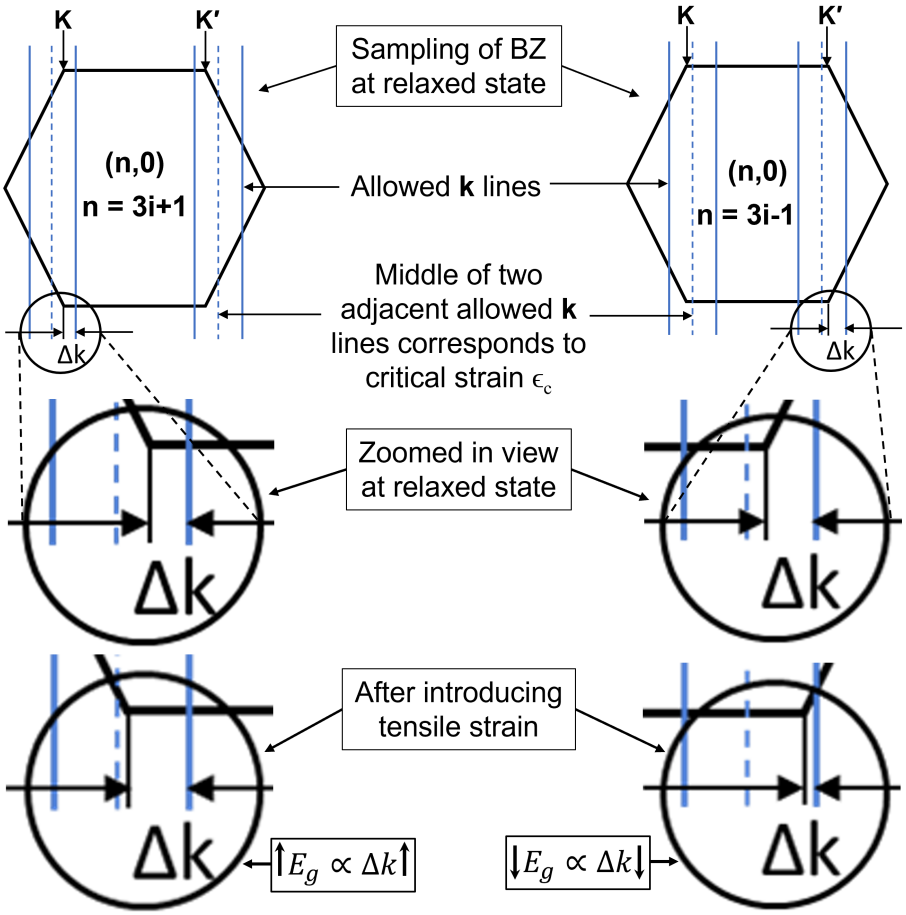

Figure S3: An exaggerated view of the sampling of irreducible first Brillouin zones of $(n, 0)$ SWCNTs, where the left column images are for $n = 3i + 1$ and the right column images are for $n = 3i - 1$. The uniaxial strain is shown for tensile strain case.

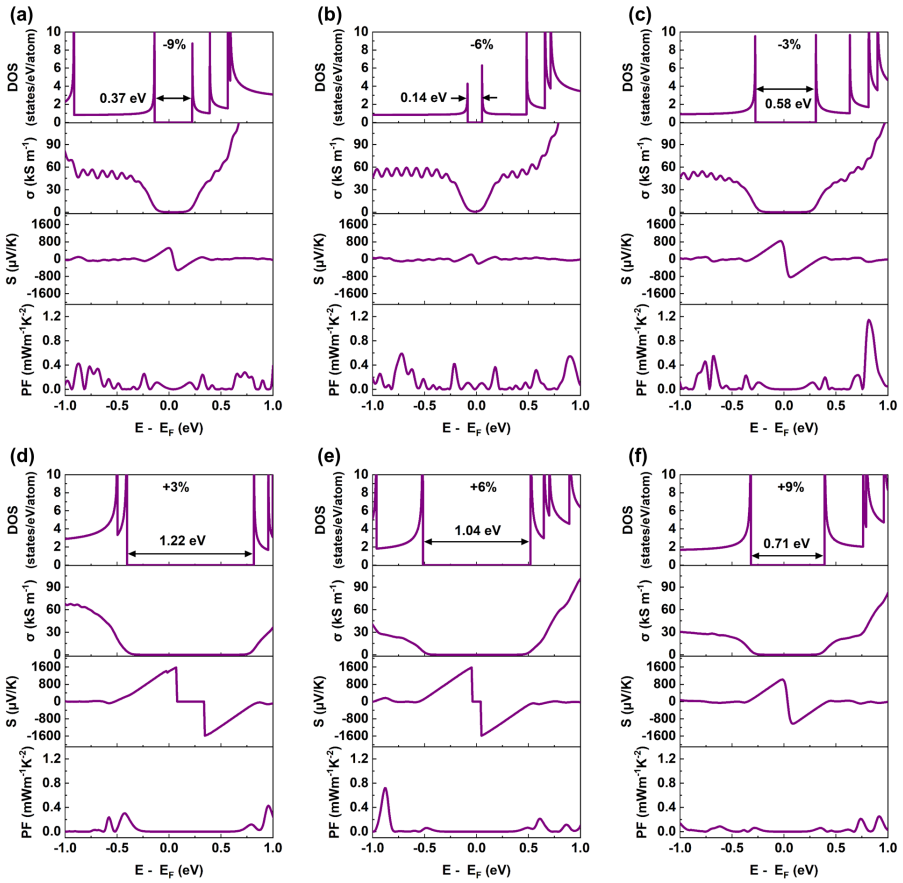

Figure S4: The electronic DOS and the calculated thermoelectric transport parameters: electrical conductivity σ, Seebeck coefficient S, and thermoelectric power factor PF as a function of chemical potential for (10,0) SWCNT at different level of uniaxial strains– (a) -9%, (b) -6%, (c) -3%, (d) +3%, (e) +6%, and (f) +9%. The Fermi level E_F is shifted to 0 eV in the energy axis.

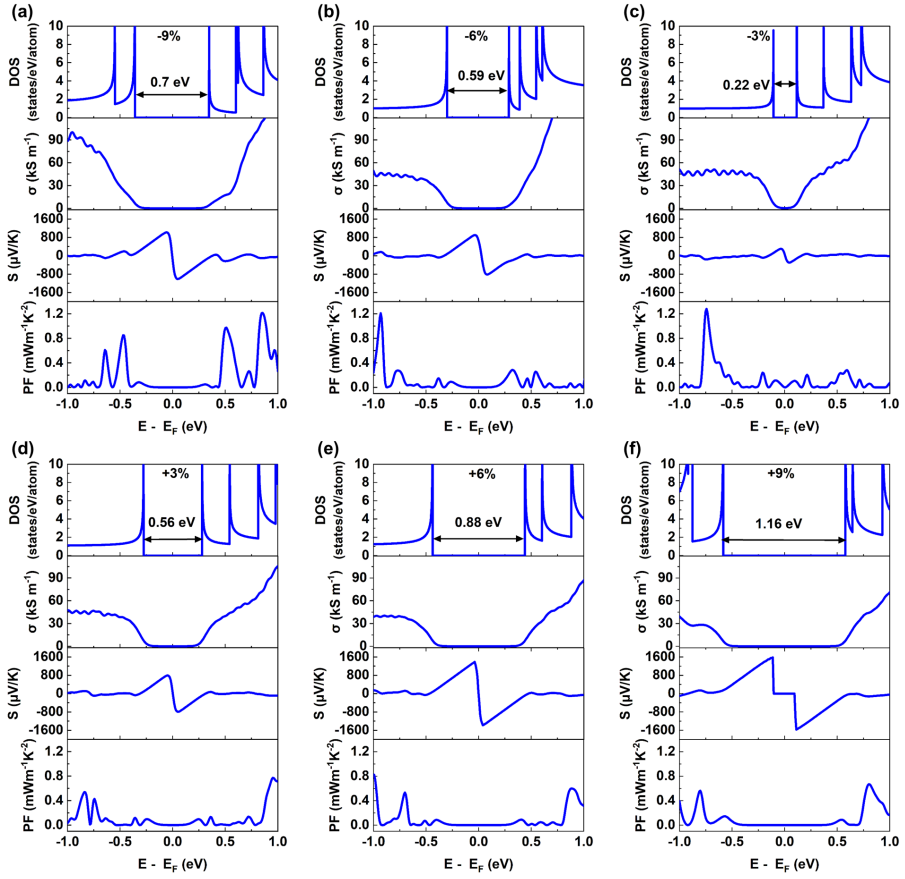

Figure S5: The electronic DOS and the calculated thermoelectric transport parameters: electrical conductivity σ, Seebeck coefficient S, and thermoelectric power factor PF as a function of chemical potential for (9,0) SWCNT at different level of uniaxial strains– (a) -9%, (b) -6%, (c) -3%, (d) +3%, (e) +6%, and (f) +9%. The Fermi level E_F is shifted to 0 eV in the energy axis.

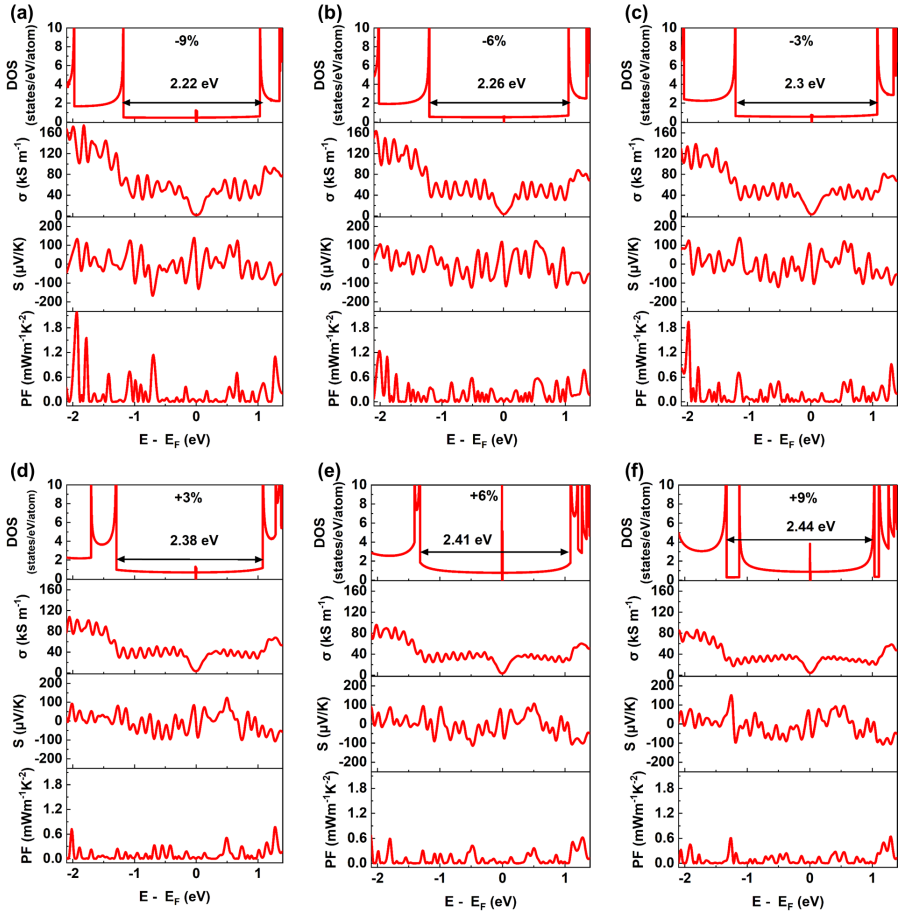

Figure S6: The electronic DOS and the calculated thermoelectric transport parameters: electrical conductivity σ, Seebeck coefficient S, and thermoelectric power factor PF as a function of chemical potential for (6,6) SWCNT at different level of uniaxial strains– (a) -9%, (b) -6%, (c) -3%, (d) +3%, (e) +6%, and (f) +9%. The Fermi level E_F is shifted to 0 eV in the energy axis.

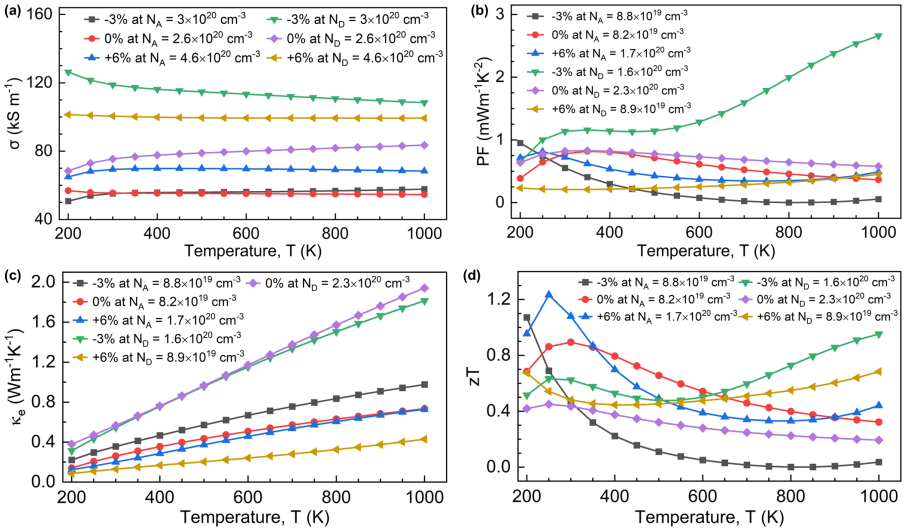

Figure S7: The calculated thermoelectric transport properties of (10,0) SWCNT as a function of temperature at different level of acceptor (N_A) and donor (N_D) concentrations. The results are shown at compressive strain (-3%), relaxed state (0%), and tensile strain (+6%) condition, where the peak value of σ, PF, zT, and minimum of κ_e were obtained.